PAN POLISH ACADEMY OF SCIENCES

Opto-Electronics Review

journal homepage: http://journals.pan.pl/opelre

Radiometric calibration and measurement algorithm for electrical inspection solar-blind ultraviolet cameras

Casper J. Coetzer[a]*, Nicholas West[b]

[a] Dept. of Electrical, Electronic and Computer Engineering, University of Pretoria, Hatfield 0028, South Africa
[b] Dept. of Electrical and Information, University of Witwatersrand, 1 Jan Smuts Ave., Braamfontein 2000, Johannesburg, South Africa

Article info

Article history:
Received 8 Oct. 2021
Received in revised form 11 Dec. 2021
Accepted 20 Dec. 2021
Available on-line 13 Feb. 2022

Keywords:
AC voltage; calibration; corona cameras; electrical discarges; radiometric measurements.

Abstract

Solar-blind ultraviolet cameras with image intensifier with CMOS detector typically use various count methodologies to measure the optical energy of an electrical corona. However, these count methodologies are non-radiometric without considering parameters such as distance, focus-, zoom-, and gain setting of a camera. An algorithm which considers the calibration and radiometric measurement of optical energy for the slow frame rate intensifier type cameras is presented. Furthermore, it is shown how these calibration data together with the flowcharts are used for the conversion from raw measured data to radiometric energy values.

1. Introduction

Solar-blind ultraviolet (SBUV) cameras and instruments using image intensifier technology are part of the preventive maintenance (detection) of high voltage transmission components [1, 2]. The most popular type of camera technology uses an image intensifier coupled detector with a CMOS detector (ICMOS) configuration [3, 4]. The number of experiments with different types of multiple and single detectors has implied that there is a relation between electrical corona loss and optical energy observed [4–7]. Unfortunately, most of the commercial SBUV ICMOS cameras are only used to provide an image without providing any indication of severity by measurements of the optical intensity [4]. The reason for this is a tendency for the commercial and research cases to use image processing techniques instead of radiometric relations to determine optical energy [4, 5].

The processing techniques for SBUV ICMOS cameras can be summarized as follows:

- Counting pulses in an image: centroiding algorithms are used to locate the point spread functions (pulses) in an ICMOS image [8, 9]. These pulses are then used as the camera count response as shown in Fig. 1. The multi-pixel sized events require centroiding algorithms each with different requirements and aspects [8]. Equal sizes of events (pulse footprint) are one such requirement which does not occur in practice.
- Pixel counting: it is a popular algorithm that is used by most of the SBUV cameras [4]. Each pixel value above a digital threshold is counted. The transfer function is similar to the multi-pixel event transfer function of Fig. 1 as described by Fordham *et al.* [10]. Our investigations implied that the problem with counting

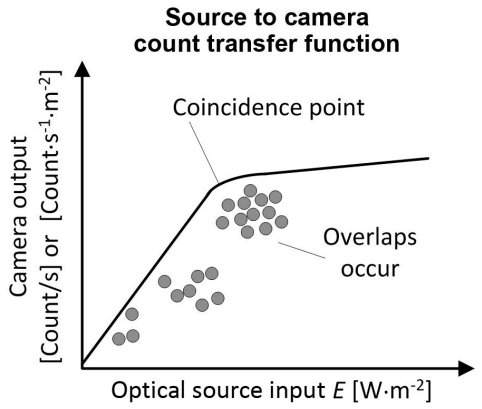

Fig. 1. Source to camera count output for image intensifier cameras.

*Corresponding author at: casper.coetzer.uv@gmail.com

https://doi.org/10.24425/opelre.2022.140128
1896-3757/ Association of Polish Electrical Engineers (SEP) and Polish Academic of Sciences (PAS). Published by PAS

was that the different camera focus positions make it difficult to attain repeatable similar measurements.

- Pixels summation and subtraction: frames of an active signal and non-signal (blank) frames are subtracted from each other and averaged [4, 11]. Personal experience with this method implied that many frames are required to obtain consistent repeatable results.

It is argued that a radiometric measurement algorithm should consider how the SBUV ICMOS camera displays images and, also, consider the response to electrical discharges. Figure 2 shows typical raw images of the SBUV ICMOS camera in a three-dimensional format.

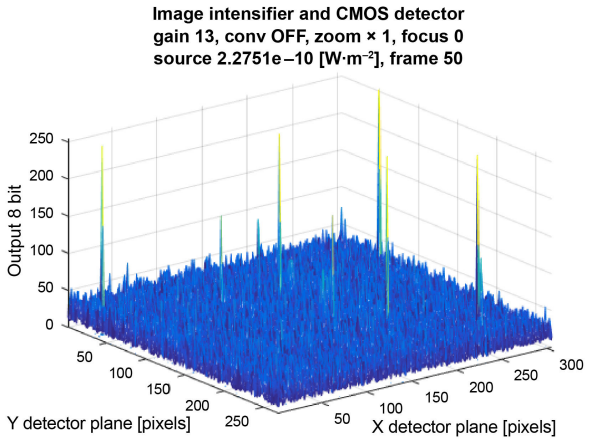

Fig. 2. Image from the image intensifier CMOS camera (Corocam 504).

It shows the background noise with a digital level of 50 presented units together with the pulses in the image. This noise is attributed to an electronic background interference (EBI) of the intensifier [3, 12]. Pulses (also referred to as events) are attributed to the phosphor response as the result of electrons hitting the anode phosphor plane of the anode of the intensifier [3, 9, 10].

Clues for a suitable radiometric algorithm for SBUV ICMOS cameras can be derived from other SBUV detectors that share similar detector technology but provide a different image output. An example is an SBUV camera with an anode resistive output which implied that optical pulses correlate with electrical corona discharge pulses over time and a relative pulse height [13]. This pulse height consideration is confirmed by the related electrical domain discharge energy (Coulomb units), which is measured by summation of pulses and their heights over a time period, as in Fig 3 [4, 14].

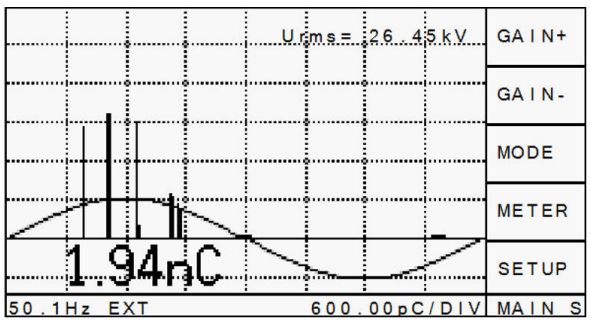

Fig. 3. Electrical partial discharge measurement of corona pulses measured with an ICM compact at University of Witwatersrand.

It is concluded that due to the dependence of electrical and optical discharge of SBUV, the optical energy measurement should not only count the pulses but should also consider the pulses heights. In addition, the optical measurement should consider a statistical variation similar to that of electrical discharge measurements, as well [15].

2. Raw (un-calibrated) measurement algorithm

2.1. *Introduction*

The first step involves the un-calibrated measurement method of the optical signal consistent with radiometric principles [16, 17].

2.2. *Rudimentary measurement relations*

The measurement methodology selected here is based on the optical energy format of the optical energy incident on the camera lens area [3, 16, 17]. This is known as irradiance (E) with the units of [W·m^{-2}] as described by:

$$E_{LENS} = \int_0^\infty \frac{\partial \phi_\lambda}{\partial A_L} d\lambda = \int_0^\infty \frac{L_\lambda \partial A_O}{r^2} \tau_\lambda \, d\lambda \qquad (1)$$

with the spectral flux ϕ_λ [W·nm^{-1}], the lens area A_L [m^2], the source spectral radiance L_λ [W·m^{-2}·sr^{-1}], the source area A_O [m^2], and the distance r between source and camera summed over the wavelength λ spectrum.

The SBUV ICMOS camera measures (observes) the incident optical energy on each detector pixel as a digital value:

$$d_{i\lambda} = \phi_{\lambda i} R_i G = \left(\frac{\varepsilon_\lambda L_{bb} d\lambda A_O A_1 \tau}{r_i^2} \right) (R_i) G \, , \qquad (2)$$

with the detector responsivity (spectrum) R, the camera gain G, the pixel area A_1 [m^2], the source spectral radiance modelled as the spectral emisivity ϵ_λ, and the blackbody L_{bb} [W·m^{-2}·sr^{-1}], the source area A_O [m^2],the distance r_i between source and camera summed over the wavelength $d\lambda$ spectrum [17]. In (2), the detector responsivity per pixel R_i general description is:

$$R_i = R_{Oi} R_{\theta i}(\theta,\phi) R(P) R_{Si}(\lambda) R_i(\lambda) R(t) \, , \qquad (3)$$

where R_{Oi} is the non-spectral output per unit flux, R_θ is the relative spatial response (field of view) with θ angle between lens boresight and pixel position [17], $R(P)$ is the relative polarity function, $R(t)$ is the relative time domain response, $R_{Si}(\lambda)$ are the camera system parameters that exclude the detector, and $R_i(\lambda)$ is the detector spectral response. It is possible to correct the non-spectral portion of the response of (2) of each camera pixel so that the response is uniform over the field of view (FOV) with:

$$R_i = R_{Oi} k_{\theta i} R_{\theta i}(\theta,\phi) k_{xy\_i} R(P) R(t) [R_{Si}(\lambda) R_i(\lambda)], \qquad (4)$$

where $k_{\theta i}$ is the pixel FOV correction factor and k_{xy_i} is the positional pixel correction factor. $k_{\theta i}$ is the digital amplitude correction factor related to the $\cos^4\theta$ amplitude, which can be obtained by a point source in a test bench [17].

Fortunately, most SBUV cameras used for electrical corona observations have a narrow FOV of about 10° [4], which is a very low distortion implying that FOV correction could be ignored for the simplified measurement algorithm (2) that contains (4). In addition, the camera settings can be included in (2) resulting in:

$$d_{i\lambda} = \phi_{\lambda i} R_i z G(f(r)) f(foc) , \tag{5}$$

with the camera zoom z (×1 or ×0.5 for the Corocam 504), the focus position $f(fov)$, the camera gain G, and the function of distance $f(r)$.

As (5) contains the flux ϕ_λ, it can be concluded that the source irradiance E can be determined by the summation of pixel values d_i. This summation methodology should also comply with the following requirements [4]:

- Summation processing technique must not be affected by the number of frame samples selected;
- Deal with fluctuations of data of consecutive frames (explored in section 2.5 and shown in Fig. 5);
- Provide a way of discrimination between the measured signal and the blank background as later discussed in section 2.5 and illustrated in Fig. 6;
- Not be affected by focus settings (Fig. 17 – section 5.3) as radio-metric measurements are not affected [16];
- Deal with camera frame rates slower and asynchronous with the 60 or 50 Hz of AC power cycle.

2.3. *Enhanced measurement relation*

The enhanced measurement uses the sum of pixels (d_{SUM}), each with the detector value d_i above the threshold of the T_{BCKG} background signal described by:

$$d_{SUM} = \sum_{i=1}^{x_i \times y_i} d_i \quad \text{for} \quad d_i > T_{BCKG} . \tag{6}$$

Alternatively, the summation of pixels of a particular selected area could be applied in the image (cluster). An example is where multiple sources or only part of electrical discharges (streamers *vs.* discharge point) are measured. The summation in this case is then:

$$d_{SUM} = \sum_{Cluster\ i=1}^{Cluster\ x_i \times y_i} d_i \quad \text{for} \quad d_i > T_{BCKG} . \tag{7}$$

2.4. *Determining the threshold (background)*

The T_{BCKG} threshold of (6) and (7) is determined by using the distribution of digital pixel values for the case of no source present (a blank input). It was determined that all pixel values for the blank case are normal distribution, which is presented in the statistical frequency format in Fig. 4 [18, 19]. In this format, it is possible to determine what most of the pixel values are by using confidence intervals (where a certain percentage of the pixel values occurs). The upper limit line of 95% is used as the T_{BCKG} threshold. All pixel values larger than T_{BCKG} are regarded as active values and used in the summation of the active image using (6) and (7).

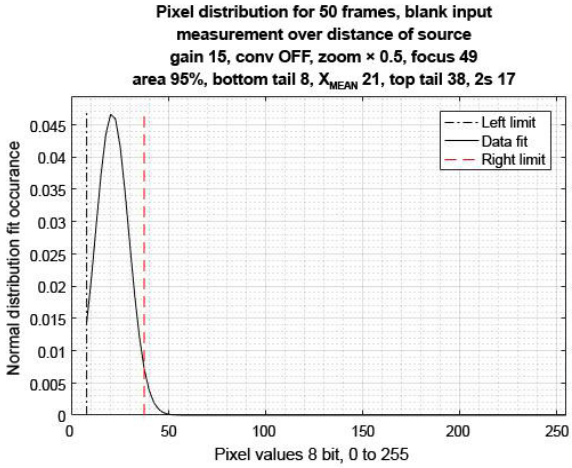

Fig. 4. Distribution of pixel values for a blanked input (no signal).

2.5. *Example of uncalibrated signal measurement*

Figure 5 shows the typical results of processing each of 50 consecutive camera frames from (6), each with a T_{BCKG} threshold of 38 pixel values in Fig. 4. The resulting measurement is the average (X_{MEAN}) of the number of frames, as well as the application of statistical rejection (above and below the confidence level of a 95% probability). Using this and other rejection methods (i.e., rank and trim), the effect of Cherenkov radiation observed as sporadic blobs and occasional frame-slip that upsets measurements (the average) can be reduced or totally eliminated [3].

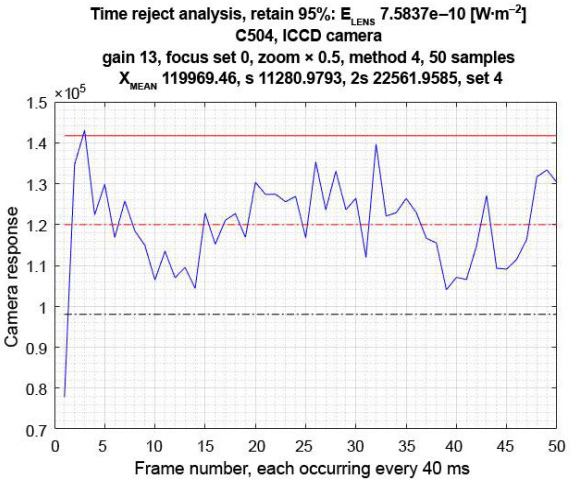

Fig. 5. Processing of 50 consecutive frames with pixel summation.

The results of Fig. 5 are shown as a normal distribution in Fig. 6. This is achieved by data ranking, which means data is arranged from small to large. This is then used to calculate the average and standard deviation, which are next used to determine the occurrence of each using the normal distribution relation [19]. The same figure also shows the blank series of the signal pixel summation. The blank signal is also a series of pixel sums for the same number of frames, but without considering the T_{BCKG} threshold. Thus, this shows how to distinguish between the two sets of data (no source *vs.* source input) setting (i.e., gain, zoom) [18, 19].

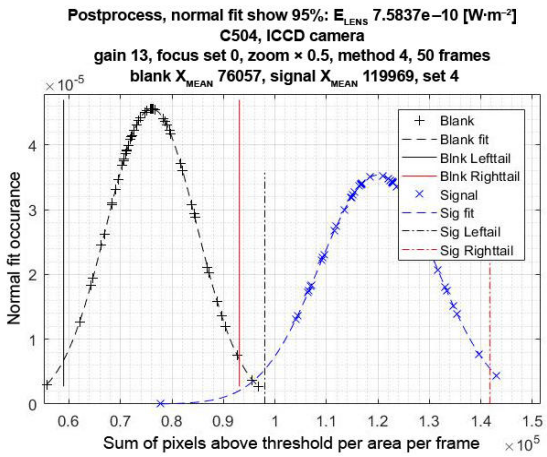

Fig. 6. Normal distribution of signal frames and distribution of blank frames (no signal).

This was also discussed and investigated in a similar manner for the counting methodology earlier by this investigative team [18].

3. Calibration algorithm

3.1. Introduction

Armed with the raw measurement relation (6) and average (X_{MEAN}) values, the next step is to calibrate the SBUV camera to make the measurement of optical energy possible. The objective of calibration is to establish the relation between the camera response (6) and the known energy source to be used by the measurement based on (5).

3.2. Calibration source

There are various types of sources that are proposed for the calibration of SBUV cameras such as Blackbody radiators, deuterium lamps, laser, electrical discharge, and specially adapted LED sources [20, 21]

SBUV cameras have different output responses to each of these sources, which are attributed to the difference between the spectrum of the source and the cameras themselves. The methods and proposals to solve the spectral mismatching will be discussed in the future as an additional step to improve accuracy. The narrowband source is used here as part of the first full calibration step.

3.3. Calibration curves

Relations (1) to (5) need to be manipulated in such a manner that the measured digital level can be converted to an optical energy flux format relation [4, 20]. However, part of the solution (source *vs*. camera output) is in the enclosed form of an integral that needs to be solved. To overcome the enclosed form, a set of source *vs*. camera responses (calibration curves) is created to measure the unknown optical energy. Figure 7 shows the concept of the set of calibration curves. It is designed for a variety of camera gain settings to overcome the enclosed format and dynamic range limitations. The dynamic calibration curves are limited at the maximum input by the number of pixels that are saturated in this particular case. Coincidence count should be used if the count algorithm is used [10].

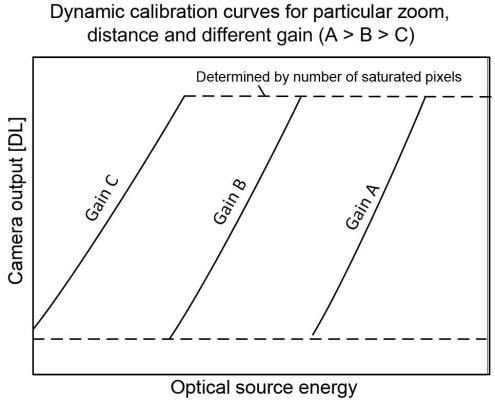

Fig. 7. Dynamic range graphs for different camera gain settings.

Experiences with wideband sources suggest that the source and camera output relation for a dynamic graph can be typically described by a second order polynomial equation. A straight-line approximation for the relation (source and camera output) to a narrow band source for the purpose of explanation used here is:

$$d_E = a_m E + c_m \,, \tag{8}$$

where d_E is the digital output of the camera using (6), a_m is the gradient coefficient, E is the known source irradiance at a particular distance, and c_m is the offset [17].

Figure 8 shows another type of a calibration set for source values at a distance for a particular camera gain and zoom setting. To be able to measure the source at different distances (narrowband and wideband source), the relation describing it was found to be:

$$d_{Er} = \frac{a_r e^{b_r r}}{r^2} + c_r \,, \tag{9}$$

where d_{Er} is the digital output of the camera (6), a_r and b_r are the coefficients at distances r and c_r is the offset for a known source irradiance E, r^2 is attributed to the attenuation with distance, and b_r is the combined atmospheric attenuation.

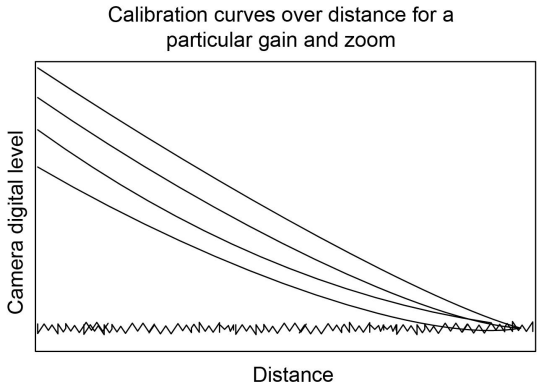

Fig. 8. Different source values over distance, the same camera settings.

Set of gain calibration curves for different source values is illustrated in Fig. 9. Each curve presents the camera output for a particular optical energy at a fixed distance for different gain settings. The digital output of the d_{Eg} camera from (6) as a function of the gain related to the typical ICMOS gain can be described by:

$$d_{Eg} = a_g e^{b_g E} + c_g \,, \tag{10}$$

where a_g and b_g are the coefficients, E is the source of irradiance at fixed distances, and c_g is the offset.

It is possible to follow various calibration measurements of the optical source.

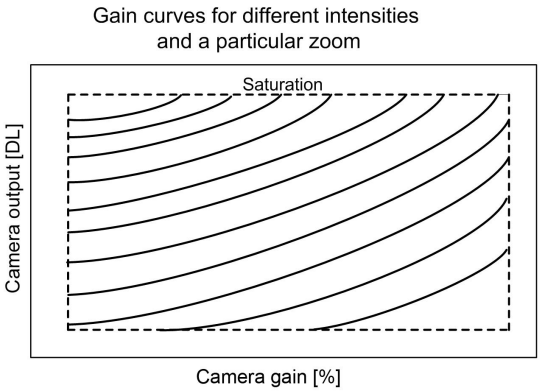

Fig. 9. The effect of gain on different values of optical energy.

3.4. *Measurement algorithm*

The optical measurement algorithm consists of two parts: an automatic gain control (AGC) with frame measurements and a calibration table lookup function. Figure 10 provides an outline of the AGC where the gain is readjusted, if required, after the number of frames, each processed from (6). Each frame is compared to the T_{BCKG} blank signal threshold (lower than the noise) to determine if the camera gain needs to be increased. To ensure that the camera gain is not too excessive, the number of saturated pixels is monitored, as well as saturated frames. The gain is decreased if the number of saturated pixels and/or frames exceeds a predetermined threshold.

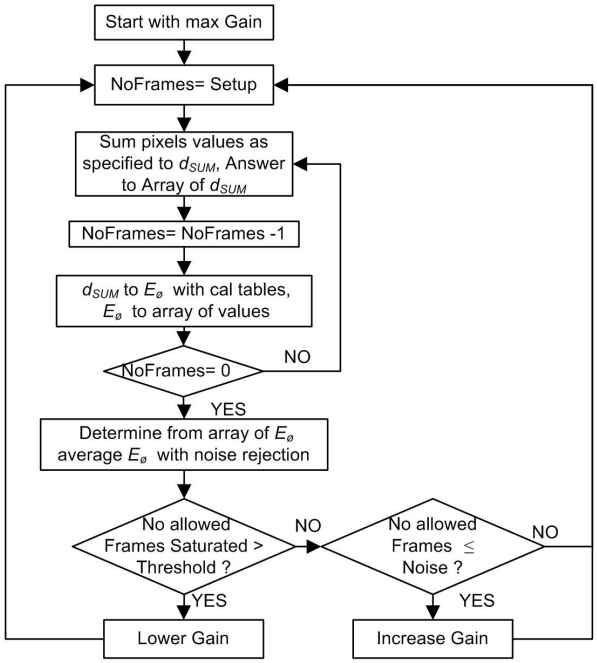

Fig. 10. Camera measurement, calibration lookup, and automatic gain control.

Following the successful measurement of consecutive frames at the optimum gain, the average value should be converted to an optical measurement. The outline of how the average (X_{MEAN}) of the frames is converted to optical energy using the calibration relations (graphs) is presented in Fig. 11. The flowchart shows how the X_{MEAN} measurement is manipulated to the calibration graph camera settings (i.e., gain, zoom, and distance) through the number of steps and then is finally converted to optical energy.

The first step is the modification of the measured average $X_{MEANMEASZ1}$ for a zoom setting of 1 or $X_{MEANMEASZ05}$ for a zoom of 0.5 to the calibration table zoom setting. This is done with one of two relations derived from (8) that is:

$$X_{MEANz05} = \left(m_{z05} m_{z1}^{-1} [X_{MEANMEASz1} - c_{z1}]\right) + c_{z05} \tag{11}$$

and

$$X_{MEANz1} = \left(m_{z1} m_{z05}^{-1} [X_{MEANMEASz05} - c_{z05}]\right) + c_{z1} \,, \tag{12}$$

where $X_{MEANz05}$ is the camera zoom setting to a multiplication of 0.5, X_{MEANz1} is the zoom of 1, c_{z05} is the offset for a zoom of 0.5, c_{z1} is the offset for a zoom of 1, m_{z05} is the gradient of output function for a zoom of 0.5, and m_{z1} is the gradient of output function for a zoom ×1.

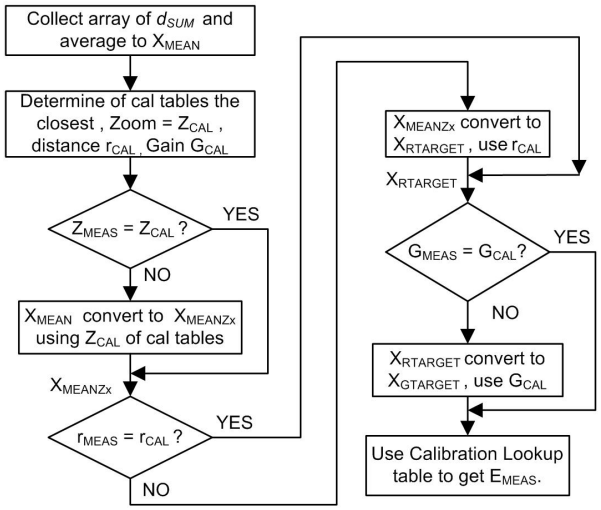

Fig. 11. Conversion of the summation of a frame pixel digital level to an optical energy format using conversion factors and calibration tables.

Next, the previous value of X_{MEANZ} at the r_{meas} distance at which the measurement was made is converted to the r_{target} target calibration curve distance. This new value is referred to as $X_{RTARGET}$ and is obtained by manipulating (9) for both distances to:

$$X_{RTARGET} = \left(r_{MEAS}^2 \cdot r_{TARGET}^{-2} [X_{MEANZ} - c_{MEAS}]\right) + c_{MEAS} \,. \tag{13}$$

The previous $X_{RTARGET}$ is then converted to the calibrated $X_{GTARGET}$ graph gain by manipulating (10) from the two gain relations (measured and calibrated) to:

$$X_{GTARGET} = \left(e^{b_g g_c} \cdot e^{-b_g g_{meas}} [X_{RTARGET} - c_g]\right) + c_g, \tag{14}$$

where the camera gain for the original frames was measured by g_{maes}, g_c is the calibration table gain, b_g is the gain constant, and c_g is the gain offset.

Finally, the $X_{GTARGET}$ value is converted to the measured optical energy value such as E by using the inverse relation (8) or alternatively using the iterative lookup in the case where the dynamic relation is a polynomial.

4. Example of calibration

4.1. Overview

This section shows the actual calibration of the SBUV camera (Corocam 504) used for the subsequent measurement.

4.2. Dynamic calibration

A typical dynamic calibration graph is presented in Fig. 12 showing the relation between the optical energy incident on the camera lens area and the camera response using (6). Each point on the graph is an X_{MEAN} of 50 frames including the signal (frame) rejection described earlier.

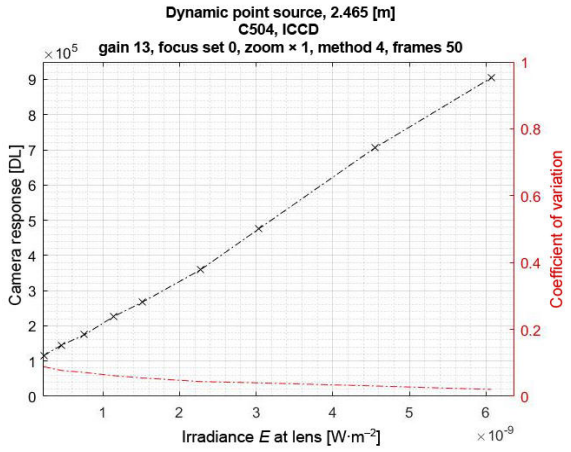

Fig. 12. Uploading dynamic calibration function in the camera setting.

4.3. Zoom calibration

Figure 13 shows two dynamic graphs for the same source values, but for different camera zoom settings (× 0.5 and ×1). Each graph can be fitted to a straight line similar to (8), that is:

$$d_{Z\times 1} = 1.3661 \times 10^{14} E + 70870 \tag{15}$$

and

$$d_{Z\times 0.5} = 3.4461 \times 10^{13} E + 96119\,. \tag{16}$$

4.4. Distance calibration

Figure 14 shows a calibration curve for a particular source energy, zoom × 0.5, and camera gain over distance. The fitted particular graph relation here is:

$$X_{RCAL} = \frac{a_r e^{b_r r}}{r^2} + c_r = \frac{346859 e^{1\times 10^{-6} r}}{r^2} + 67938\,. \tag{17}$$

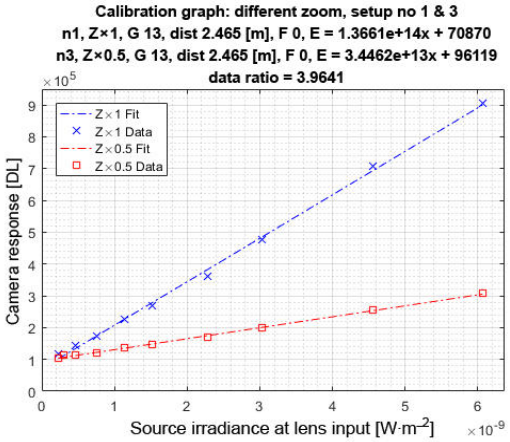

Fig. 13. Uploading dynamic calibration function in different camera zoom settings.

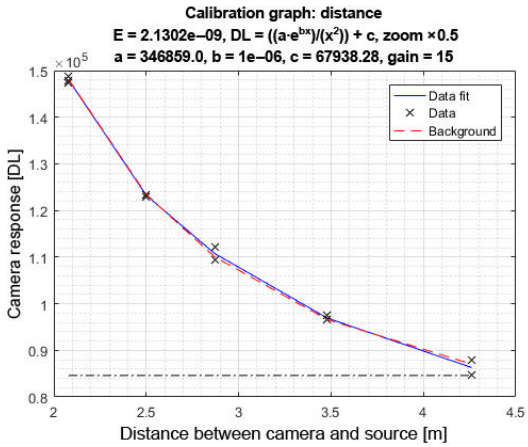

Fig. 14. Calibration graph showing the effect of measuring the same source energy at different distances.

4.5. Gain calibration

Figure 15 shows an example of the gain graph described by:

$$X_{GCAL} = a_G e^{b_G G} + c_G = 2407.8 e^{0.067 G} + 96118\,, \tag{18}$$

based on (10). This calibration curve can only be used up to a 50% gain as there are too many saturated pixels above a 60% gain. It should be noted that the 0.067 factor closely corresponds to the gain result of Wang *et al.* [7] of 0.074.

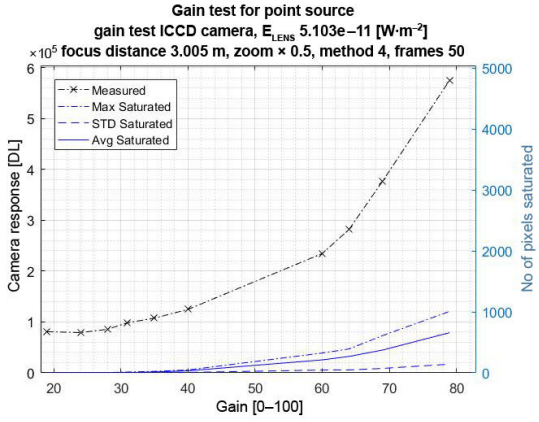

Fig. 15. Calibration graph showing the effect of measuring the same source energy at different gain settings of a camera.

5. Calibration checks and balances

5.1. Introduction

Illustrated here is how a calibration and measurement algorithm can be evaluated by using calibration or known measured source data as input.

5.2. Dynamic evaluation

Figure 16 shows that the input to output relation is unity (1:1), implying that the measurement algorithm result is correct. The data used is the actual calibration data to verify the unity relation of the measurement algorithm.

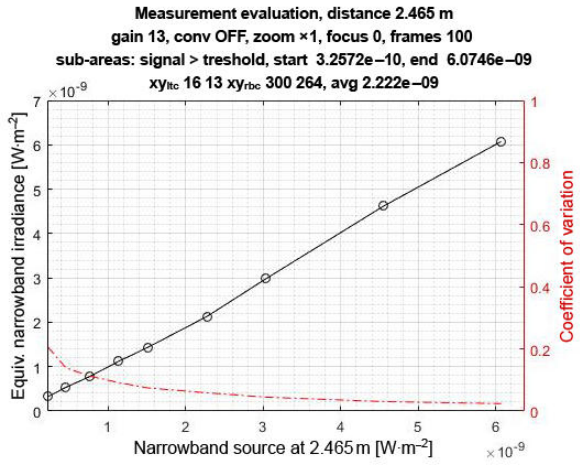

Fig. 16. Dynamic evaluation of the measurement algorithm resulting in an input to the output ratio of 1 to 1 with a known calibrated source input.

5.3. Focus evaluation

Next, the ability to be insensitive to different camera focus settings is investigated in Fig. 17. It is illustrated with some success but highlights that the measurement algorithm starts to struggle to focus above 60%. The reason for this is that the image becomes smaller at the higher focus settings with saturated pixel values. It can be concluded that the measurement insensitivity to focus positions is at least better than a counting algorithm. Unfortunately, measurements must be rejected above a 60% focus where the pixel saturation occurs.

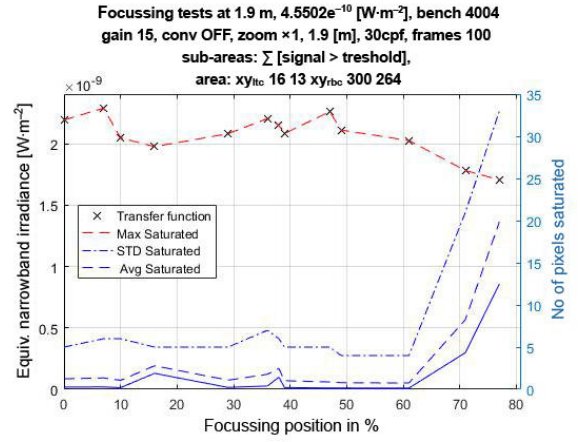

Fig. 17. Energy measured at different camera focus settings.

5.4. Distance evaluation

Figure 18 shows that the measurement algorithm provides the same measurement at different distances if each measurement is transferred (projected) to the first observation distance. This is of course only a special test routine of the measurement and not what happens with actual irradiance measurements as shown in Fig. 19.

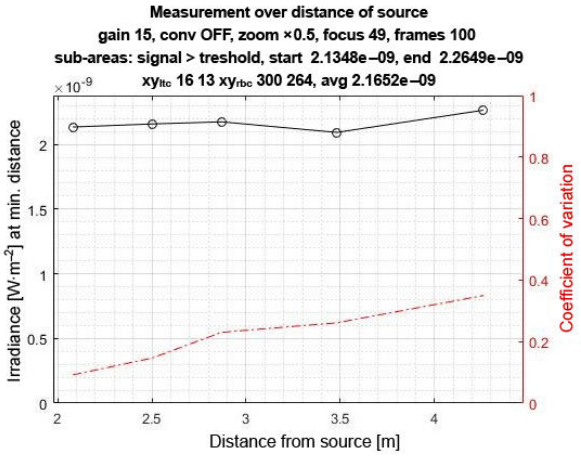

Fig. 18. Energy measurement translated to a fixed reference distance.

It is possible to prove that the measured optical energy (irradiance) decreases with distance as shown next in Fig. 19. This corresponds with the description (relation) of irradiance over distance [3, 16]:

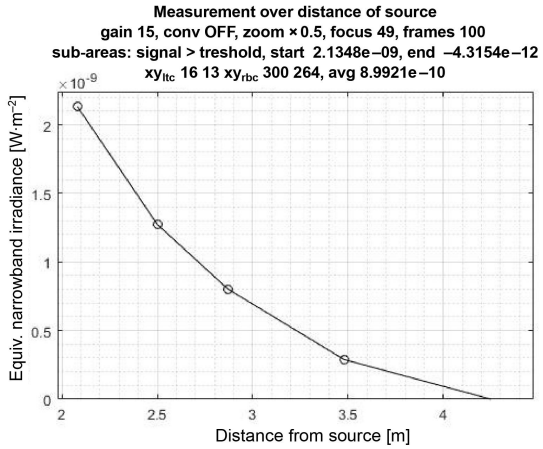

Fig. 19. Determining if the decrease in optical irradiance energy with distance is detectable with the measurement algorithm.

6. Application measurement

6.1. Introduction

Presented here is an example of how the SBUV ICMOS camera can measure optical energy (radiometric measurement) as part of an electrical experiment.

6.2. Electrical test example

Figure 20 shows that it is possible to measure the SBUV of an electrical discharge using the calibration and measurement methodology as summarized in the flow

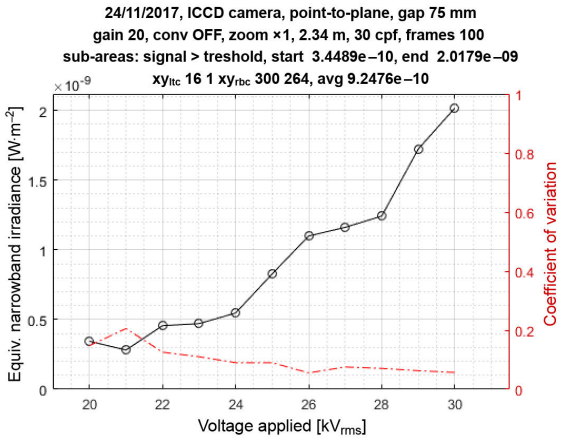

Fig. 20. The solar-blind ultraviolet optical energy detected from an electrical point-to-plane corona discharge.

diagrams of Fig. 10. and Fig. 11. Each point of the graph here consists of 100 frames that each was used to perform the optical measurement. The measurement shows the optical energy equivalent to a narrowband calibration source used here for the Corocam 504 SBUV camera.

The coefficient of variation (CV) is also shown for each measurement, implying that there is less than 20% variation of the signal [18, 19].

7. Conclusions

For the first time it was highlighted here that most SBUV ICMOS cameras used to observe corona discharges lack a true radiometric measurement ability. The previous investigation by the author with another camera detector technology, such as the resistive anode, has suggested that the methods using pulse or pixel counting are inadequate as the height of the pulses should also be considered. These new insights are used as part of the algorithm presented here for the current imaging SBUV ICMOS cameras.

The calibration method is also demonstrated here with the calibration source. Calibration curves for a specific gain, zoom, focus, and distance settings are included along with their mathematical relations. The radiometric measurement algorithm using a rudimentary model was used. More parameters (i.e., lens distortion over the FOV) should provide more accurate results. The measurement algorithm converts the measurement which had a certain camera setting to the calibration curve camera settings to perform a radiometric measurement. Furthermore, it was shown how it is possible to verify the accuracy of the measurement algorithm with known data for different camera settings. Finally, an actual measurement example was shown with the electrical parameter and the optical energy measurement relation.

The algorithm is not only applicable for ICMOS type cameras but also for other types of camera detectors such as the resistive anode. Note that the role of the spectral bandwidth of the source and camera was not addressed in this simplified measurement algorithm. The consideration for spectrum will be presented in the future.

References

[1] Gubanski, S., Dernfalk, A., Andersson, J. & Hillborg, H. Diagnostic methods for outdoor polymeric insulators. *IEEE Trans. Dielectr. Electr. Insul.* **14**, 1065–1080 (2007). https://doi.org/10.1109/TDEI.2007.4339466

[2] Lindner, M., Elstein, S., Lindner, P., Topaz, J. M. & Phillips, A. J. Daylight corona discharge imager. in *1999 11th International Symposium on High Voltage Engineering* 349–352 (London, 1999). https://doi.org/10.1049/cp:19990864

[3] Bass, M. *et al*. *Handbook of Optics, Volume II: Design, Fabrication and Testing, Sources and Detectors, Radiometry and Photometry*. (McGraw-Hill, Inc., 2009).

[4] Coetzer, C. *et al*. Status quo and aspects to consider with ultraviolet optical versus high voltage energy relation investigations. in *5th Conference on Sensors, MEMS, and Electro-Optic Systems* 1104317 (Skukuza, South Africa, 2019). https://doi.org/10.1117/12.2501251

[5] Maistry, N., Schutz, R. A. & Cox, E. The quantification of corona discharges on high voltage electrical equipment in the uv spectrum using a corona camera. in *2018 International Conference on Diagnostics in Electrical Engineering (Diagnostika)* 1–4 (Pisen, Czech Republic, 2018). https://doi.org/10.1109/DIAGNOSTIKA.2018.8526024

[6] Dai, R., Lu, F. & Wang, S. Relation of composite insulator surface discharge ultraviolet signal with electrical pulse signal. in *2011 International Conference on Electrical and Control Engineering* 282–285 (Wuhan, China, 2011). https://doi.org/10.1109/ICECENG.2011.6056830

[7] Wang, S., Lv, F. & Liu, Y. Estimation of discharge magnitude of composite insulator surface corona discharge based on ultraviolet imaging method. *IEEE Trans. Dielectr. Electr. Insul.* **21**, 1697–1704 (2014). https://doi.org/10.1109/TDEI.2014.004358

[8] Suhling, K., Airey, R. W. & Morgan, B. L. Optimisation of centroiding algorithms for photon event counting imaging. *Nucl. Instrum. Methods Phys. Res. B* **437**, 393–418 (1999). https://doi.org/10.1016/S0168-9002(99)00770-6

[9] Boksenberg, A., Coleman, C., Fordham, J. & Shortridge, K. Interpolative centroiding in CCD-based image photon counting systems. *Adv. Electron. Electron. Phys.* **64**, 33–47 (1986). https://doi.org/10.1016/S0065-2539(08)61601-7

[10] Fordham, J., Moorhead, C. & Galbraith, R. Dynamic-range limitations of intensified CCD photon-counting detectors. *Mon. Notices Royal Astron. Soc.* **312**, 83–88 (2000). https://doi.org/10.1046/j.1365-8711.2000.03155.x

[11] Coetzer, C. J. & Leuschner, F. W. The influence of a camera's spectral transfer function used for observing high voltage corona on insulators. *IEEE Trans. Dielectr. Electr. Insul.* **23**, 1753–1759 (2016). https://doi.org/10.1109/TDEI.2016.005021

[12] Hamamatsu Photonics, K. K. *Photomultiplier tubes: Basics and applications. Edition 3a.* https://www.hamamatsu.com/content/dam/hamamatsu-photonics/sites/documents/99_SALES_LIBRARY/etd/PMT_handbook_v3aE.pdf (2007).

[13] Coetzer, C., Becker, T., West, N. & Leuschner, W. Investigating an alternate detector for solar-blind ultraviolet cameras for high-voltage inspection. in *2021 Southern African Universities Power Engineering Conference/Robotics and Mechatronics/Pattern Recognition Association of South Africa (SAUPEC/RobMech/PRASA)* 1–6 (2021). https://doi.org/10.1109/SAUPEC/RobMech/PRASA52254.2021.9377216

[14] IS/IEC 60270:2000 Indian Standard, *High Voltage Test Techniques-Partial Discharge Measurements.* (International Electrotechnical Commission, 2000).

[15] Tang, J., Luo, X. & Pan, C. Relationship between PD magnitude distribution and pulse burst for positive coronas. *IET Sci. Meas. Technol.* **12**, 970–976 (2018). https://doi.org/10.1049/iet-smt.2018.5039

[16] Willers, C. J. *Electro-Optical System Analysis and Design: A Radiometry Perspective*. (Society of Photo-Optical Instrumentation Engineers, 2013). https://doi.org/10.1117/3.1001964

[17] Wyatt, C. *Radiometric Calibration: Theory and Methods*, (Elsevier, 2012).

[18] Coetzer, C., Groenewald, S. & Leuschner, W. An analysis of the method for determining the lowest sensitivity of solarblind ultraviolet corona cameras. in *2020 International SAUPEC/RobMech/ PRASA Conference* 1–6 (Cape Town, South Africa, 2020). https://doi.org/10.1109/SAUPEC/RobMech/PRASA48453.2020.9040997

[19] Montgomery, D. C. & Runger, G. C. *Applied Statistics and Probability for Engineers*. (John Wiley and Sons, 2014).

[20] Coetzer, C., West, N., Swart, A. & van Tonder, A. An investigation into an appropriate optical calibration source for a corona camera. in *2020 International SAUPEC/RobMech/PRASA Conference* 1–5 (IEEE, Cape Town, South Africa, 2020). https://doi.org/10.1109/SAUPEC/RobMech/PRASA48453.2020.9041014

[21] Chrzanowski, K. & Chrzanowski, W. Analysis of a blackbody irradiance method of measurement of solar blind UV cameras' sensitivity. *Opto-Electron. Rev.* **27**, 378–384 (2019). https://doi.org/10.1016/j.opelre.2019.11.009